IOP Publishing Measurement Science and Technology
Meas. Sci. Technol. **31** (2020) 055005 (12pp) https://doi.org/10.1088/1361-6501/ab60c7

Attitude estimation of a permanent magnet spherical motor based on an improved fast discriminative scale space tracking algorithm

Lei Xue[1,2], Qunjing Wang[1,2,3], Siliang Lu[1,2], Guoli Li[1,2] and Runyu Tang[1,2]

[1] College of Electrical Engineering and Automation, Anhui University, Hefei, Anhui 230601, People's Republic of China
[2] National Engineering Laboratory of Energy-Saving Motor and Control Technology, Anhui University, Hefei, Anhui 230601, People's Republic of China

E-mail: wangqunjing@ahu.edu.cn

Received 10 July 2019, revised 4 December 2019
Accepted for publication 11 December 2019
Published 31 January 2020

Abstract

A permanent magnet spherical motor (PMSM) can perform a three-degree-of-freedom operation. The estimation of the attitude of the rotor is one of the key steps for realizing the closed-loop control of PMSM. An attitude estimation method based on a target-tracking algorithm is proposed in this study. Firstly, a high-speed camera is used to capture a video sequence of the spherical motor in motion. The location of the target is obtained by introducing an improved fast discriminative scale space tracking (IFDSST) algorithm to track the video sequence. In consideration of the motor's output shaft being covered with load, the single-target tracking algorithm is improved into a multi-target tracking algorithm. Markers, which are symmetrical with respect to the output shaft, are made on the surface of the rotor, and their attitudes are obtained from the images captured by the tracking algorithm. Secondly, the attitude of the output shaft is estimated by the coordinate transformation and the positional relationship between the markers and the output shaft. The effectiveness and superiority of the proposed algorithm are verified by comparing it with a micro-electromechanical system (MEMS) method and a fast -complementary filter (FCF) method. Three types of motor motions, including yaw, spin, and tilt, are tested in the experiments, and the average angle error or trajectory error of the proposed IFDSST method reduces around 33%, 53%, and 79% as compared with those of the MEMS and FCF methods, respectively. Experiments show that the proposed algorithm can effectively and accurately measure the attitude of the motor's rotor.

Keywords: permanent magnet spherical motor, attitude estimation, target tracking

(Some figures may appear in colour only in the online journal)

1. Introduction

With the development of industrial control and the continuous advancement of science and technology in the last few decades, multi-dimensional movement in space has been required in more applications, such as in eyeballs, joints of humanoid robots, and other precision devices [1–3]. Traditional multi-degree-of-freedom (DOF) implementation relies on multi-DOF systems consisting of multiple single-DOF motors and complex mechanical transmissions. Moreover, the loss caused by friction between devices cannot be neglected, and the realization of low loss operation has always been one of the goals

[3] Author to whom any correspondence should be addressed.

of high-power industries [4–6]. However, such a multi-DOF system has the disadvantages of bulky volume, low precision, and poor performance. Therefore, a single motor with multi-DOF must be studied in detail to identify the best electrical machine among the above applications in terms of cost and technology [7–9]. From a kinematic point of view, the spherical structure of a motor is conducive to the realization of spatial multi-axis drive, which is a three-DOF motor, and can overcome the various shortcomings of traditional multi-DOF systems by replacing them with several single-DOF motors [10–12].

Much attention has been paid to spherical motors by many researchers. Despite the merits of a permanent magnet spherical motor (PMSM), further studies on closed-loop feedback control for spherical motors are needed. Precision attitude measurement is a key technology for achieving closed-loop control [13–15]. Attitude information is extremely important for the accuracy of motor motion control, orientation control, and processing [16–18]. Moreover, attitude and speed information are two of the most important parameters for motor system control and early diagnosis purposes [19–21]. The method of attitude estimation and the selection of its sensors largely determines the success and accuracy of attitude estimation. In accordance with whether the sensor is in contact with the sphere, attitude estimation methods of the spherical motor are divided into contact- and non-contact-type detection.

The contact-type detection method is mainly to install the rotary encoder on the slide rail bracket [22, 23]. The attitude information of the rotor is measured by rotating the encoder. However, the large size of the measuring device can affect the range of the motion of the rotor. The most important thing is that the contact between the detection system and the rotor generates great friction, which not only weakens the output torque of the motor rotor, but also affects the detection accuracy. Therefore, when high precision and reliability are required, non-contact detection methods are generally used [24]. A non-contact attitude estimation method, which mainly uses photoelectric sensors to detect spherical surface color signals to obtain rotor attitude, was proposed [25, 26]. However, this method increases the complexity of the system, and it is difficult to realize accurate spraying on the rotor surface. In [22], Garner *et al* proposed the use of a vision sensor to acquire the attitude of the rotor. The specific method is to spray the grid diagram on the rotor surface according to the pseudo-random method. After the rotor image is obtained by the visual sensor, the feature points of the image are extracted, so as to analyze and obtain the rotor position. In [27], Lee *et al* presented the use of dual optical sensors to detect the surface variation of the rotor in both directions to obtain the 3D attitude information of the rotor. In addition, a Hall sensor was used to detect the distribution and variation of magnetic field around the rotor to calculate the spatial position of the rotor [28]. However, the magnetic field generated by the energized coil will interfere with the Hall sensor to some extent, thus affecting the attitude detection of the rotor.

Given the advantages and disadvantages of the above methods and the trade-offs of previous work, a novel attitude estimation method for the spherical motor rotor, which is a non-contact method, is proposed in this study. The method includes marking the motor using a high-speed camera to obtain the motor motion video, and applying the improved fast discriminative scale space tracking algorithm (IFDSST) to track the marks and obtain the position in the image. Through the coordinate transformation and the positional relationship between the mark and the output shaft, the actual attitude of the output shaft is obtained. The contributions of this study include three aspects as follows.

(1) The attitude of PMSM is estimated by the non-contact method, which can avoid the influence of friction caused by the contact between the sensor and the motor in attitude detection.
(2) The method is simple in structure and the camera sensor is not affected by the changing magnetic field around the PMSM.
(3) The accuracy of the proposed IFDSST for the attitude estimation of PMSM is higher than those of the micro-electromechanical system (MEMS) sensor and the fast complementary filter (FCF) using an integral sensor including a magnetic sensor, an angular rate sensor and a gravity sensor (MARG) [29], which are verified through experiments.

The rest of the paper is organized as follows: section 2 introduces the structure of the PMSM and the establishment of the stator coordinate system. Section 3 presents the fast discriminative scale space tracking (FDSST) algorithm and its improvement. Section 4 shows the calculation method for the attitude angle of the rotor. Section 5 verifies the effectiveness and accuracy of the proposed algorithm, and section 6 provides the conclusions.

2. PMSM structure and coordinate system

The basic structure of the PMSM used in this study is shown in figure 1. It is composed of a stator coil and a spherical rotor. Twenty-four sets of stator coils are divided into the upper and lower layers and evenly distributed on the spherical shell. Forty cylindrical permanent magnets are evenly placed on the motor's rotor, which is divided into four layers with ten magnets per layer. The radiuses of the rotor and the output shaft are 65 mm and 4 mm, respectively. The length of the output shaft is 40 mm. These parameters are helpful for calculating the rotor's attitude angle.

The established stator coordinate system is shown in figure 2 to describe the attitude of the rotor concisely and accurately. The coordinate system is based on the center of the rotor sphere. The equatorial plane is taken as the *XOY* plane, and the positive direction of the *Z*-axis is opposite to the gravity direction. The motion state of PMSM is mainly divided into three types: yaw, spin, and tilt. In figure 2, the letters α, β, and γ are defined as the yaw, spin, and tilt angle, respectively. P is the intersection of the output shaft and the rotor sphere. P' is the projection point of P on the *XOY* plane. The initial state of the motor is defined as the position where

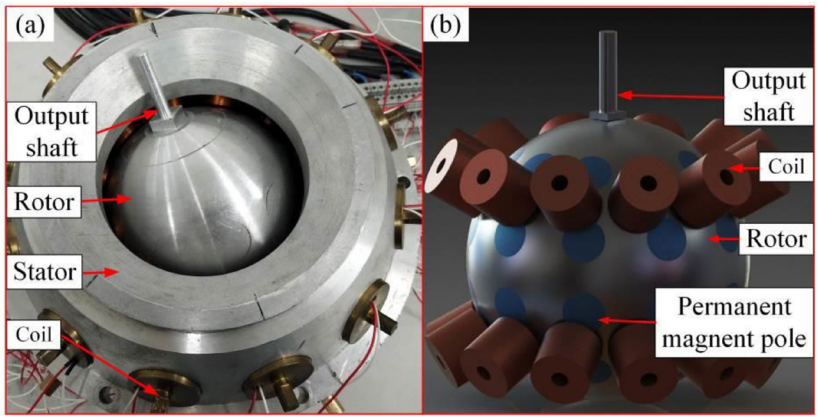

Figure 1. Basic structure of the PMSM: (a) prototype of the PMSM, (b) 3D model of the PMSM.

the output shaft lies with the *Z*-axis; that is, the initial attitude of the upper end surface of the output shaft is (0, 0, 105).

3. IFDSST algorithm for tracking detection

3.1. Traditional FDSST algorithm

Target tracking is a hot topic in the field of computer vision research. With the continuous improvement in computer hardware, target tracking has been increasingly applied to military and industrial fields, such as video surveillance and motion analysis [30–32]. In recent years, the target tracking algorithm based on correlation filter not only is highly robust but also ensures real-time tracking performance [33–35].

FDSST implements scale-adaptive tracking based on the correlation filter [36]. Details are as follows. The desired output is obtained through the target in the first frame interacting with the translation correlation filter. The detected samples extracted in each frame interact with the translation and scale filters, respectively, and the response of the detected sample is compared with the expected output. The maximum value is considered the displacement and scale produced by the target movement.

The FDSST algorithm is based on a discriminant correlation filter. This tracking algorithm is mainly divided into three steps: translation estimation, scale estimation, and filter update. The target detected in the previous frame is used as a training sample for filter update in the next frame. The histogram of the oriented gradient (HOG) feature is extracted from samples before training and detection. In an image, the directional density distribution of the gradient or edge can well describe the appearance and shape of the local target. The HOG feature constitutes a feature by calculating and counting a gradient direction histogram of a local region of the image. The extracting process of HOG feature is shown in figure 3. Extracting HOG feature first grayscales and normalizes the image. Normalization is to adjust the contrast of the image and reduce the effects of local shadows and changes in illumination. Then the gradient of each pixel in the image, including size and direction, is calculated, primarily to capture contour information and further attenuate illumination interference. The image is divided into a number of cells, each cell

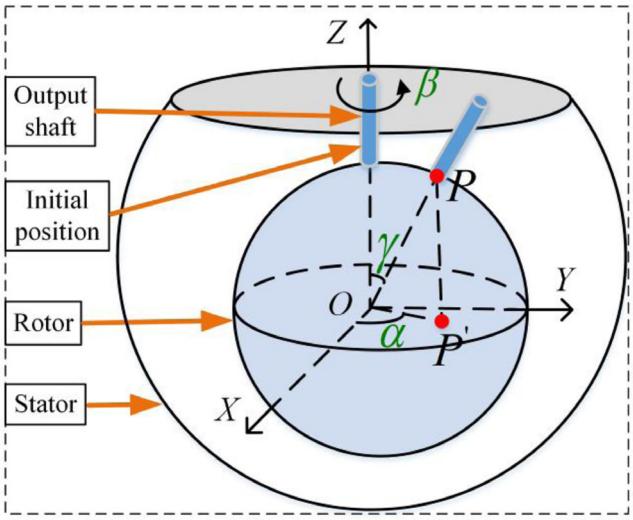

Figure 2. Stator coordinate system.

consisting of several pixels, such as $6 * 6$ pixels forming a cell as shown in figure 4(b). In figure 4(a), 360° are divided into several bins, and the histogram of the gradient of each pixel is calculated in each cell by direction. The modes of these gradients are added to obtain the components of the corresponding bin. If the 360° are divided into 16 bins, the dimension of the histogram for each cell is 16. Cell features are constituted by these histograms. The cells are combined into a number of blocks, and these cell features are connected in a series to form a block feature as shown in figure 4(b). If a block contains $2 * 2$ cells, the dimension of the block feature is $16 \times 4 = 64$. The HOG feature of the image is obtained by concatenating these block features.

In general, the initial position of the target generates a Gaussian label and initializes template parameters for the target. For a target sample with a d-dimensional feature channel, the correlation filter consists of d single-channel filters, which can be solved by minimizing the objective function ε as

$$\varepsilon = \left\| g - \sum_{l=1}^{d} h^l * f^l \right\|^2 + \lambda \sum_{l=1}^{d} \left\| h^l \right\|^2, \tag{1}$$

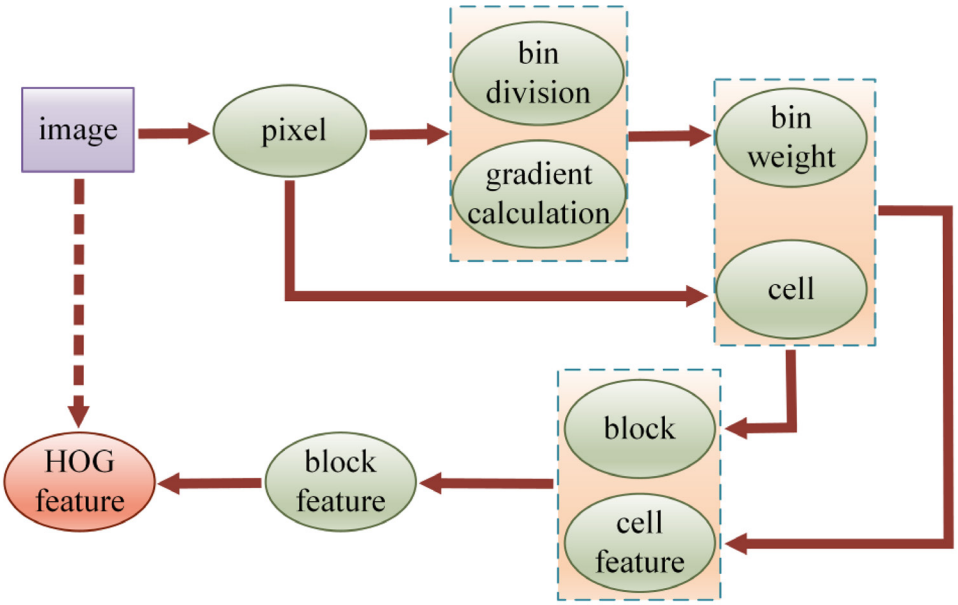

Figure 3. The extracting process of the HOG feature.

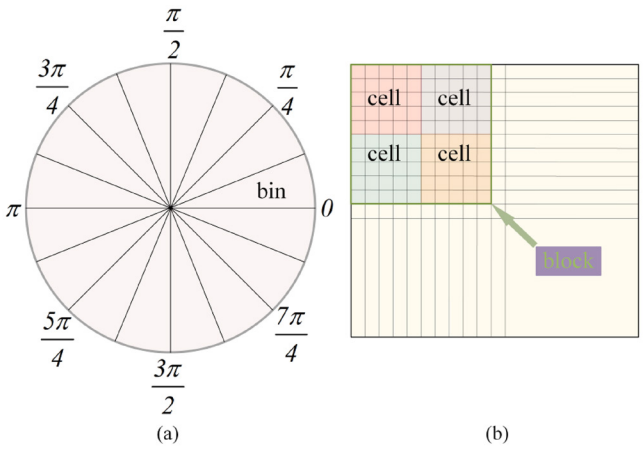

Figure 4. (a) Bin, (b) cell and block.

where g is the expected output of the correlation filter, h is the correlation filter, f is the target sample, $l \in \{1, ..., d\}$ denotes the feature channel, $*$ refers to the cyclic correlation, and ε is the L^2 error, which is the correlation response compared to the desired correlation output g. The scalar λ is a weight parameter in the second term as regularization in (1). Equation (1) can be solved quickly by Fourier transform using Parseval's formula as follows:

$$H^l = \frac{\overline{G}F^l}{\sum_{k=1}^{d} \overline{F^k}F^k + \lambda}, l = 1, ..., d, \tag{2}$$

where the capital letters indicate the discrete Fourier transform (DFT) of the corresponding quantities, $\overline{G}$ refers to the complex conjugate, and $k \in \{1, ..., d\}$ denotes the feature channel. Inspired by the update rule of the single feature case, for a new sample f_t in a frame t, we update numerator A and denominator B of filter H as below:

$$A_t^l = (1 - \eta) A_{t-1}^l + \eta \overline{G} F^l, l = 1, \ldots, d, \tag{3}$$

$$B_t = (1 - \eta) B_{t-1} + \eta \sum_{k=1}^{d} \overline{F_t^k} F_t^k, \tag{4}$$

where the scalar η is a learning rate parameter; A_{t-1} and B_{t-1} are the numerator and denominator of the filter in the previous frame $t - 1$, respectively.

The filter is applied to a new frame by extracting the detected sample z_t from a region of transformations. For the detection sample z_t, the DFT of the correlation output response y_t is calculated in the frequency domain as follows:

$$Y_t = \frac{\sum_{l=1}^{d} \overline{A_{t-1}^l} Z_t^l}{B_{t-1} + \lambda}. \tag{5}$$

The correlation score of z_t is $y_t = \mathcal{F}^{-1}\{Y_t\}$ via inverse DFT. $\mathcal{F}^{-1}$ represents inverse DFT. The new target position is obtained when the output response reaches the maximum value.

The amount of computation is reduced by using two strategies in FDSST: sub-grid interpolation of correlation scores and the reduction of feature dimensions using principle component analysis. The amount of computation can be decreased by reducing the size of fast Fourier transforms (FFTs) required for training and detection with sub-grid interpolation. A triangular polynomial interpolation method is used. First, the high frequency of Y_t is filled in (5) to make it equal to the size of the interpolation grid. Then, the interpolation fraction y_t is obtained by the inverse DFT of Y_t after filling.

The computational cost caused by FFTs is reduced by updating a target template. The projection matrix P_t of size $\tilde{d} \times d$ is constructed by the learned template $u_t = (1 - \eta)u_{t-1} + \eta f_t$ and $\tilde{d}$ is the compressed feature dimension. P_t is obtained by

$$C_t = \sum_n u_t(n)\, u_t(n)^T. \tag{6}$$

Table 1. Flow of the proposed IFDSST algorithm.

Algorithm. IFDSST: iteration at frame t	
Input	Image $I_{t,i}$.//i denotes current target number Previous target position $p_{t-1,i}$ and scale $s_{t-1,i}$ Translation model $\tilde{A}_{t-1,i,trans}$ and $\tilde{B}_{t-1,i,trans}$ Scale model $\tilde{A}_{t-1,i,scale}$ and $\tilde{B}_{t-1,i,scale}$
Output	Estimated target position $p_{t,i}$ and scale $s_{t,i}$ using (12) Updated translation model $\tilde{A}_{t,i,trans}$, $\tilde{B}_{t,i,trans}$ and scale model $\tilde{A}_{t,i,scale}$, $\tilde{B}_{t,i,scale}$ using (10) and (11)

The row vector of P_t is a feature vector corresponding to the maximum eigenvalue of C_t. Thus, the numerator and denominator of the filter are updated as follows:

$$\tilde{A}_t^l = \overline{G}\tilde{U}_t^l, l = 1, ..., \tilde{d}, \tag{7}$$

$$\tilde{B}_t = (1-\eta)\,\tilde{B}_{t-1} + \eta \sum_{k=1}^{\tilde{d}} \overline{\tilde{F}_t^k}\tilde{F}_t^k, \tag{8}$$

where $\tilde{F}_t = \mathcal{F}\{P_t f_t\}$ and $\tilde{U}_t = \mathcal{F}\{P_t u_t\}$ are the detected samples and target templates compressed in the frequency domain, respectively. The symbol $\mathcal{F}$ represents DFT. The correlation score of the sample z_t after compression $\tilde{Z}_t = \mathcal{F}\{P_{t-1} z_t\}$ can be calculated as

$$Y_t = \frac{\sum_{l=1}^{\tilde{d}} \overline{\tilde{A}_{t-1}^l}\tilde{Z}_t^l}{\tilde{B}_{t-1} + \lambda}. \tag{9}$$

3.2. Proposed IFDSST algorithm

When the motor is applied in practice, the output shaft will be covered and cannot be directly tracked because of the load. Therefore, multi-target tracking is proposed on the basis of the single-objective FDSST algorithm, and filter models are built for each target in every frame for model training and target detection. Thus, equations (7) and (8) should be written as

$$\tilde{A}_{t,i}^l = \overline{G}\tilde{U}_{t,i}^l, l = 1, ..., \tilde{d}, \tag{10}$$

$$\tilde{B}_{t,i} = (1-\eta)\,\tilde{B}_{t-1,i} + \eta \sum_{k=1}^{\tilde{d}} \overline{\tilde{F}_{t,i}^k}\tilde{F}_{t,i}^k, \tag{11}$$

where i is the number of the target. The output response of test samples $z_{t,i}$ should be changed as follows:

$$Y_{t,i} = \frac{\sum_{l=1}^{\tilde{d}} \overline{\tilde{A}_{t-1,i}^l}\tilde{Z}_{t,i}^l}{\tilde{B}_{t-1,i} + \lambda}. \tag{12}$$

The specific method is described as follows: symmetrical markers are placed on the motor sphere, and the attitude of the motor output shaft is obtained by tracing the markers. In the following experiments, we select two circular markers that are symmetrical to the Z-axis at the initial state of the motor. In this manner, real-time tracking performance can be ensured, and the error caused by the deformation of the markers' rotation can be reduced. The algorithm flow is shown in table 1.

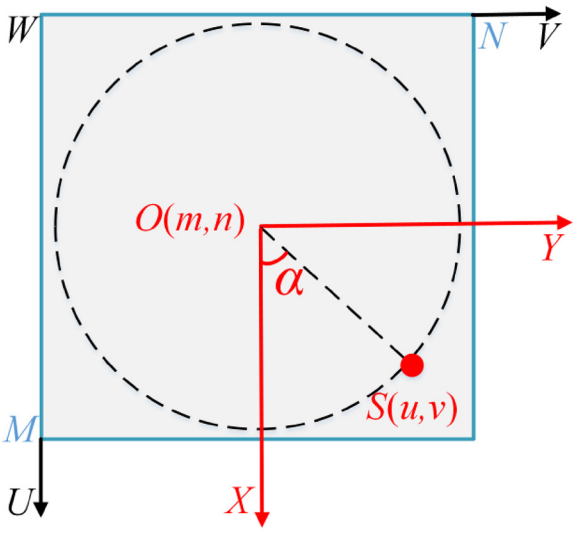

Figure 5. Image coordinate system and schematic of yaw angle calculation.

4. Motor's attitude angle calculation

4.1. Calculation of yaw angle

For yaw angle calculation, the conversion of the image and stator coordinate systems is required. The image coordinate system is based on pixel size, and its relationship with the stator coordinate system is shown in figure 5. The XOY plane belongs to the stator coordinate system, and the UWV plane is the image coordinate system. The shaded part is assumed to be the image, and the size of the image is assumed to be $M \times N$. The origin O of the stator coordinate system is located at an arbitrary point (m, n) in the UWV coordinate system. The dashed line indicates the trajectory of the output shaft of the motor during yaw motion. The point $S\,(u, v)$ represents the position of the output shaft on the image at a certain moment. Therefore, the position of S in the stator coordinate system is as follows:

$$x = (u - m) \times \mathrm{d}x, \tag{13}$$

$$y = (v - n) \times \mathrm{d}y. \tag{14}$$

Here, dx and dy are the pixel sizes of the row and column on the image, respectively. They have the same units, usually in microns. The letters x and y represent the coordinates of X-axis and Y-axis of S in the XOY plane, respectively. In accordance with figure 5 and equations (13) and (14), the yaw angle α_0 is calculated as follows:

$$\alpha_0 = \arctan\left(\frac{y}{x}\right) = \arctan\left(\frac{(v-n)\times \mathrm{d}y}{(u-m)\times \mathrm{d}x}\right). \tag{15}$$

In experiments, the point O is usually placed in the center of the image. Therefore, as shown in figure 5, the point S will not coincide with O when the motor makes yaw motion. In other words, u is not equal to m. And dx is not equal to 0. Thus, equation (15) holds true for the motor at any position. The output shaft in different quadrants is distinguished by expressing the yaw angle α in the range of 0–2π:

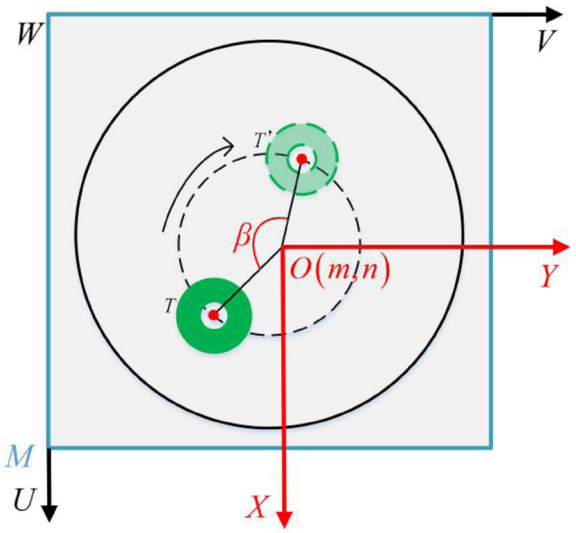

Figure 6. Schematic of spin angle calculation.

$$\alpha = \begin{cases} \alpha_0, & \text{the first quadrant} \\ \pi - \alpha_0, & \text{the second quadrant} \\ \pi + \alpha_0, & \text{the third quadrant} \\ 2\pi - \alpha_0, & \text{the fourth quadrant} \end{cases}. \tag{16}$$

4.2. Calculation of spin angle

The calculation of the spin angle is similar to that of the yaw angle. When the motor spins, the output shaft rotates around the *Z*-axis, and the attitude of the rotor is constant. Therefore, the spin angle can only be calculated by the marks, as shown in figure 6, where T is the mark in the initial position, and T' is the position of the mark when the motor rotates with spin angle β. Thus, as shown in figure 6, the calculation of the spin angle of the output shaft is converted into the difference between the yaw angles of T and T' as follows:

$$\beta = \alpha_T - \alpha_{T'}, \tag{17}$$

where α_T represents the angle between line segment OT and X-axis and $\alpha_{T'}$ represents the angle between line segment OT' and X-axis, which are all calculated by (16). The spin angle is calculated from markers that are different from the center of the end face of the output shaft. When the motor spins, the output shaft is theoretically in the initial position. The projection of the center of the end face of the output shaft in the XOY plane coincides with point O. The positions of markers do not overlap with O. Therefore, equation (15) still holds true for any point in the spin angle calculation.

4.3. Calculation of tilt angle

Details for the tilt angle calculation can be found in [14]. A schematic of tilt angle calculation is showed in figure 7. The cylinder at the top of the image represents the high-speed camera, and the thick black lines inside represent the camera's sensor. The ball at the bottom of the picture represents the rotor of the motor, and the blue cylinder connected to the rotor represents the output shaft. The center of the sensor coincides with the center of the rotor.

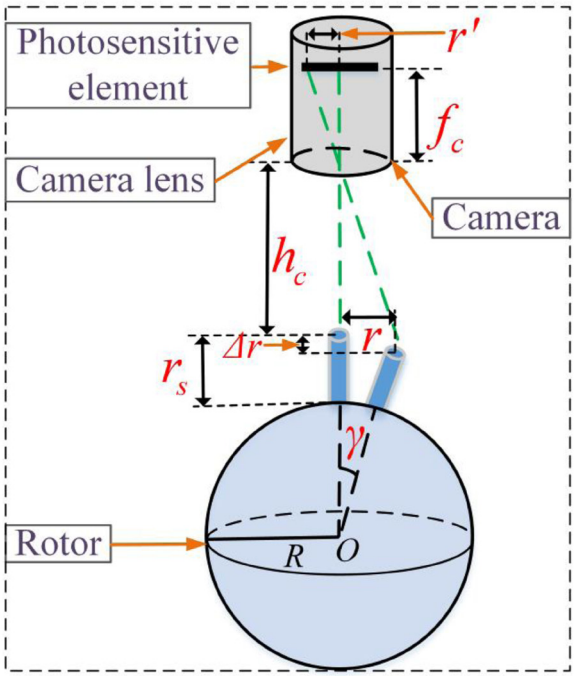

Figure 7. Schematic of tilt angle calculation.

From figure 7, the geometric relationship can be obtained as follows:

$$\frac{f_c}{h_c + \Delta r} = \frac{r'}{r}, \tag{18}$$

$$r' = \sqrt{[(u-m) \times \mathrm{d}x]^2 + [(v-n) \times \mathrm{d}y]^2}, \tag{19}$$

$$\Delta r = (R + r_s)(1 - \cos\gamma), \tag{20}$$

$$r = (R + r_s)\sin\gamma, \tag{21}$$

where f_c is the focal length, h_c is the effective distance from the lens to the rotor, r is the distance from the output shaft to the Z-axis, r' is the length of r on the image, Δr is the reduced height of the output shaft, R is the radius of the rotor, and r_s is the length of the output shaft.

Tilt angle γ_0 can be solved as

$$\gamma_0 = \arcsin\frac{r' \times [h_c + (R + r_s)]}{R + r_s + \sqrt{{f_c}^2 + {r'}^2}} - \arctan\frac{r'}{f_c}. \tag{22}$$

Since R, r_s, f_c and r' are not equal to 0, equation (22) holds true. In all experiments, the focal length of the camera f_c will be fixed. The length r' is calculated by the proposed algorithm, and h_c is the distance between the experimental equipment, which is artificially set. In general, a fixed value of h_c is taken to eliminate the error caused by the experimental devices. The quadrant of the output shaft ranges from 0–2π; thus, the tilt angle γ is expressed as follows:

$$\gamma = \begin{cases} \gamma_0, & \text{the first quadrant} \\ \pi - \gamma_0, & \text{the second quadrant} \\ \pi + \gamma_0, & \text{the third quadrant} \\ 2\pi - \gamma_0, & \text{the fourth quadrant} \end{cases}. \quad (23)$$

In the previous section, the detection principle of the algorithm was discussed to obtain the position of the rotor on the image. In this section, the method of calculating the rotor's actual attitude based on the image position information is discussed. In section 5, the accuracy of the attitude angle calculation method discussed above will be analyzed. Moreover, the topic of how to improve the precision will be discussed.

5. Experimental result

5.1. Experimental setup

All experiments in this study are performed on a desktop computer configured as an Intel(R) Core(TM) i7-6700 CPU @ 3.41 GHz with 8 GB memory. The experimental algorithm development platform is based on MATLAB R2017b. The high-speed camera (2F04, Agile Device Inc.) used in the experiments acquires an image with pixel size dx and dy as 7 μm. To ensure the repeatability of the experiments, we set the resolution to 1200 × 1200 pixels, the focal length f_c to 17 mm, and the distance from the lens to the rotor h_c to 525 mm.

The experiments are compared with the MEMS sensor detection method to verify the feasibility of the proposed algorithm [13]. The MEMS sensor is a kind of space motion processing device. It is an inertial component sensor with the advantages of low cost and low power consumption. In [13], a MPU6050 attitude sensor is used in the attitude detection system, integrating a three-axis rate gyroscope and a three-axis accelerometer. Moreover, the experimental results are compared with another quaternion-based attitude estimator with a MARG sensor array. The sensor consists a of three-axis gyroscope, accelerometer and magnetometer, and the detection results are fused together to estimate the attitude of rigid body through FCF [29]. The magnetometer is not available because the variation of the magnetic field around the PMSM is complex and uneven. Therefore, in the following experiments, the results from the gyroscope and accelerometer, which are obtained by the MEMS sensor, are fused together to solve the motor's attitude through FCF.

The experimental hardware platform is shown in figure 8(a). As shown in figure 8(b), we place circular markers on the MEMS sensor device and select two of the symmetric markers as targets for tracking, such as 1 and 3 or 2 and 4. Figure 8(c) shows the MEMS sensor equipment and its size. The MEMS sensor device is mounted on the output shaft. 10 mm represents the length of the bearing assembly between the sensor device and the output shaft. 62 mm is the length of the sensor device outside the output shaft. These two parameters are used in the calculation of the attitude angle in the experiments. On the basis of the platform, three experiments are completed: the yaw, spin, and tilt motion experiments.

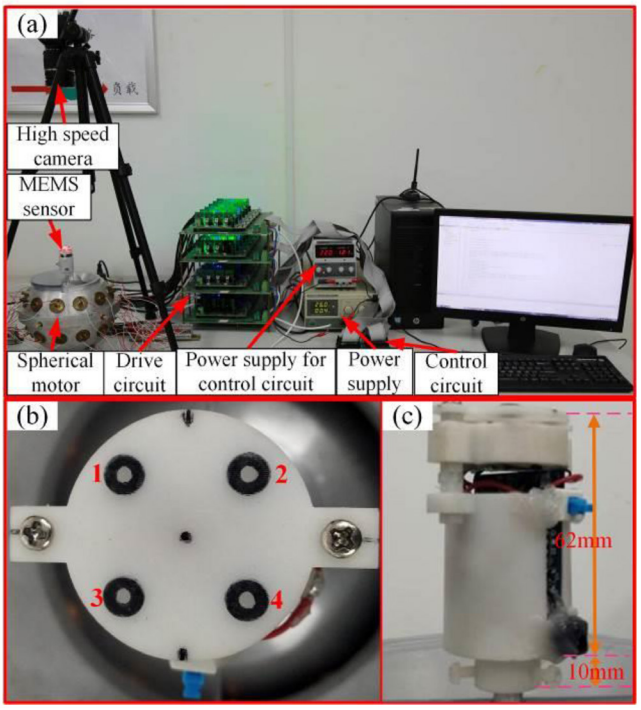

Figure 8. (a) Experimental hardware platform, (b) round marks, (c) MEMS sensor.

5.2. Yaw motion experiment

The yaw motion is the operation of the motor rotating around the Z-axis at a constant angle departing from the Z-axis. The motor makes yaw motion when the output shaft is against the stator shell. Figure 9 provides some images in the video sequence of the yaw operation. The yellow numbers on the upper left corner of the images represent the frame numbers. The red rectangles indicate the tracking results. The direction of the red dotted arrow indicates the direction of motion of the rotor. The two red rectangles are the markers, which are tracked in the video sequence. The images reveal that the targets can be successfully and accurately detected and tracked.

The trajectories obtained through the experiment are plotted in figure 10, which shows that trajectories obtained by the three measurement methods are consistent. Since the output shaft is close to the stator shell for yaw motion, the measured trajectories of the output shaft are approximately circular. This also mutually verified the validity and accuracy of the three detection methods for the position detection of PMSM. To verify the accuracy of IFDSST in yaw angle detection, we allow the motor to make yaw motions with yaw angles of 90°, 180° and 270°. The yaw angles and errors measured by the three algorithms are shown in table 2. It can be seen that the errors measured by the three methods are smaller and less

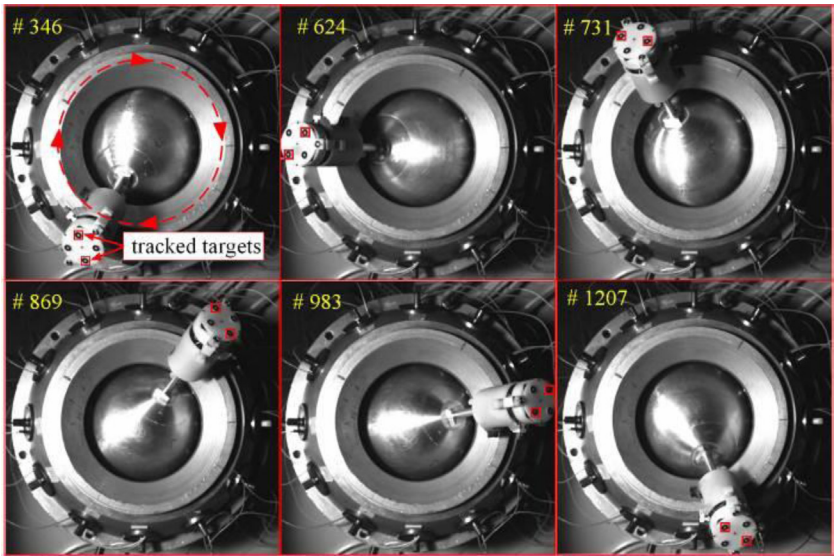

Figure 9. Some images from the video sequence of yaw motion.

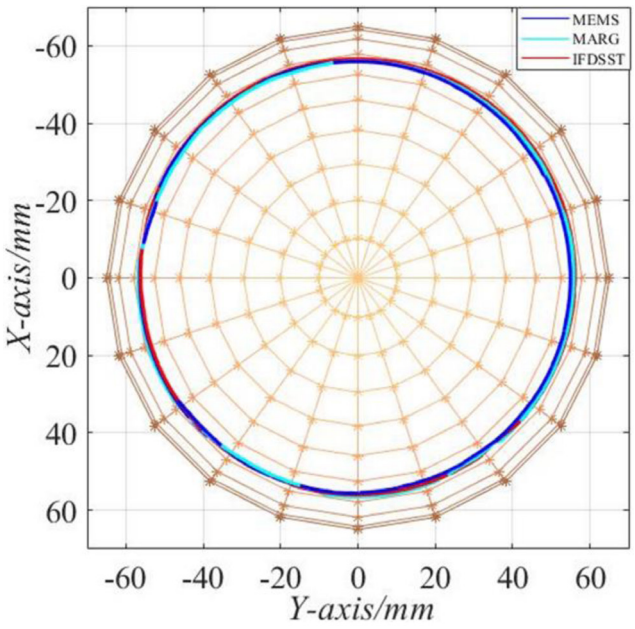

Figure 10. Trajectories from the MEMS sensor, FCF and the proposed IFDSST method in the yaw motion experiment (top view).

Table 2. Results and errors of yaw angle from the MEMS sensor, FCF and the proposed IFDSST method.

Method	Theory (°)	90	180	270	Average error (%)
MEMS	Angle (°)	88.374	177.271	266.922	—
	Error (%)	1.807	1.516	1.140	1.487
FCF	Angle (°)	88.353	177.169	267.037	—
	Error (%)	1.830	1.572	1.097	1.499
IFDSST	Angle (°)	89.185	177.936	267.294	—
	Error (%)	**0.906**	**1.147**	**1.002**	**1.018**

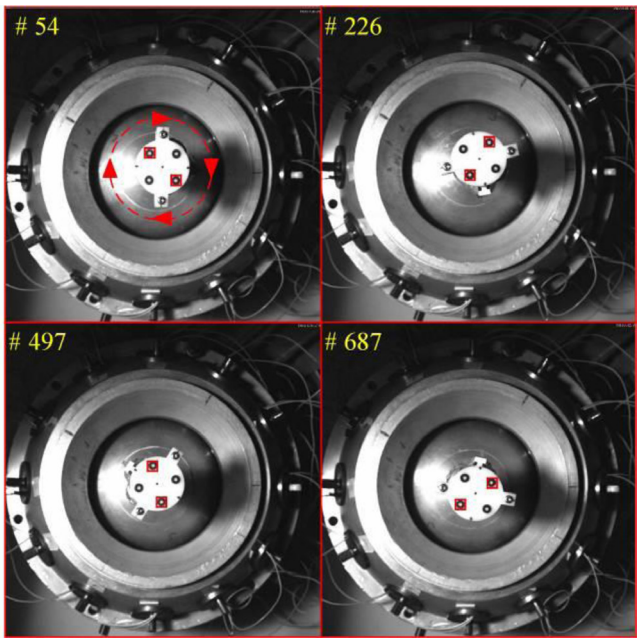

Figure 11. Some images from the video sequence of spin motion.

than 2% compared with the theoretical values. However, the average error of IFDSST is only 1.018% while those of the MEMS sensor and FCF are close to 1.5%. Thus the proposed IFDSST has higher measurement accuracy for the yaw angle.

5.3. Spin motion experiment

During the spin motion, the motor's output shaft rotates around the *Z*-axis, and the center of the end face is always in the initial attitude. Therefore, when the motor makes a spin motion, the attitude (0, 0, 105) of the center of the output shaft remains unchanged. Some images from the video sequence of

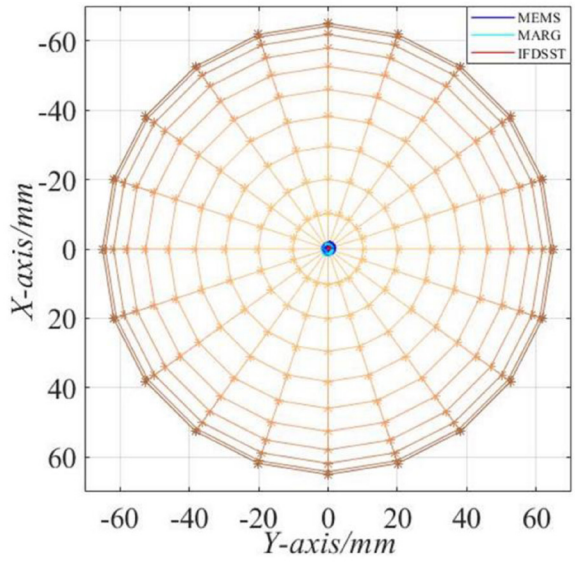

Figure 12. Trajectories from the MEMS sensor, FCF and the proposed IFDSST method in the spin motion experiment (top view).

Table 3. Means and errors of spin attitude from the MEMS sensor, FCF and the proposed IFDSST method.

Axis		*X*-axis	*Y*-axis	*Z*-axis
Theory (mm)		0	0	105
MEMS	Attitude (mm)	0.0497	0.6339	104.9928
	Error (%)	—	**0.606**	—
FCF	Attitude (mm)	−0.2281	0.6900	104.9902
	Error (%)	—	**0.692**	—
IFDSST	Attitude (mm)	−0.1573	0.2805	104.9920
	Error (%)	—	**0.306**	—

the spinning operation are presented in figure 11. The direction of the red dotted arrow indicates the direction in which the rotor makes a spin motion. As can be seen from figure 11, the proposed algorithm can track the makers robustly.

Figure 12 shows the experimental measurements. Obviously, the trajectory of the proposed algorithm is closer to the initial position. However, the results of the MEMS and FCF are deviated from the initial position. The average values of the attitude on the *X*, *Y*, and *Z* axes are shown in table 3. The error is calculated by

$$\Delta = \frac{\sqrt{(x_m - x_t)^2 + (y_m - y_t)^2 + (z_m - z_t)^2}}{\sqrt{x_t^2 + y_t^2 + z_t^2}}, \quad (24)$$

where (x_m, y_m, z_m) is the measured attitude, and (x_t, y_t, z_t) is the theoretical attitude. None of the three methods has an error of more than 1%. Within the allowable range of error, it can be considered that the three methods are effective and accurate. However, the error of the proposed method, which is closed to 0.3%, is half of those of MEMS sensor and FCF approximately. The accuracy of estimation of the spin angle using the proposed method is evaluated by spinning with angles of 90°, 180° and 270°. The MEMS sensor cannot measure the spin angle; thus, only the measurement results of the proposed algorithm are provided in table 4. In addition, the errors are no more than 1.5%.

Table 4. Results and errors of spin angle for the proposed IFDSST method.

Theoretical value (°)	Experimental value (°)	Error (%)
90	88.793	1.341
180	181.973	1.096
270	267.682	0.859

5.4. Tilt motion experiment

Tilt motion refers to the operation of the motor departing from the *Z*-axis. In this experiment, we move the motor in four directions: the positive (*X*+) and negative (*X*−) directions of the *X*-axis and the positive (*Y*+) and negative (*Y*−) directions of the *Y*-axis. For all tilt movement, the starting point of the output shaft is at the initial attitude. Some images from the video sequences of the tilt operations in the four directions are provided in figure 13. In the four pictures in each row of figure 13, the motor makes tilt motion in one direction and the red arrow indicates the direction of movement of the motor.

The measured trajectories are shown in figure 14. In four directions, the trajectories obtained by the MEMS sensor, FCF and the proposed algorithm are basically coincided. More precisely, the trajectories of the output shaft are on the lines $x = 0$ and $y = 0$ in theory. As can be seen from figure 14, the measured results of the proposed algorithm are more consistent with the theoretical results. The root mean square error (RMSE) is defined to characterize the degree of dispersion for the measured positions. In the *X*-axis direction, whatever the value of x_t is, y_t is equal to 0 for each position (x_t, y_t) theoretically. Therefore, the RMSE σ_x of the 2D positions (x_m, y_m) of all measured results in the *X*-axis direction is shown below:

$$\sigma_x = \sqrt{\frac{1}{N}\sum_{w=1}^{N} y_{m,w}^2}, \quad (25)$$

where N is the number of measured positions, and $y_{m,w}$ represents the *Y*-axis value of the w-th measured position. In the same way, the RMSE σ_y in the *Y*-axis direction is shown below:

$$\sigma_y = \sqrt{\frac{1}{N}\sum_{w=1}^{N} x_{m,w}^2}, \quad (26)$$

where $x_{m,w}$ represents the *X*-axis value of the wth measured position. All the RMSEs in four directions for the MEMS sensor, FCF and IFDSST are shown in table 5. As can be seen, the RMSEs of the proposed IFDSST are significantly smaller than those of MEMS sensor and FCF in the four directions. The average RMSEs for the MEMS sensor and FCF are around 1%, but that of the IFDSST is only 0.229%. This is also consistent with the results shown in figure 14.

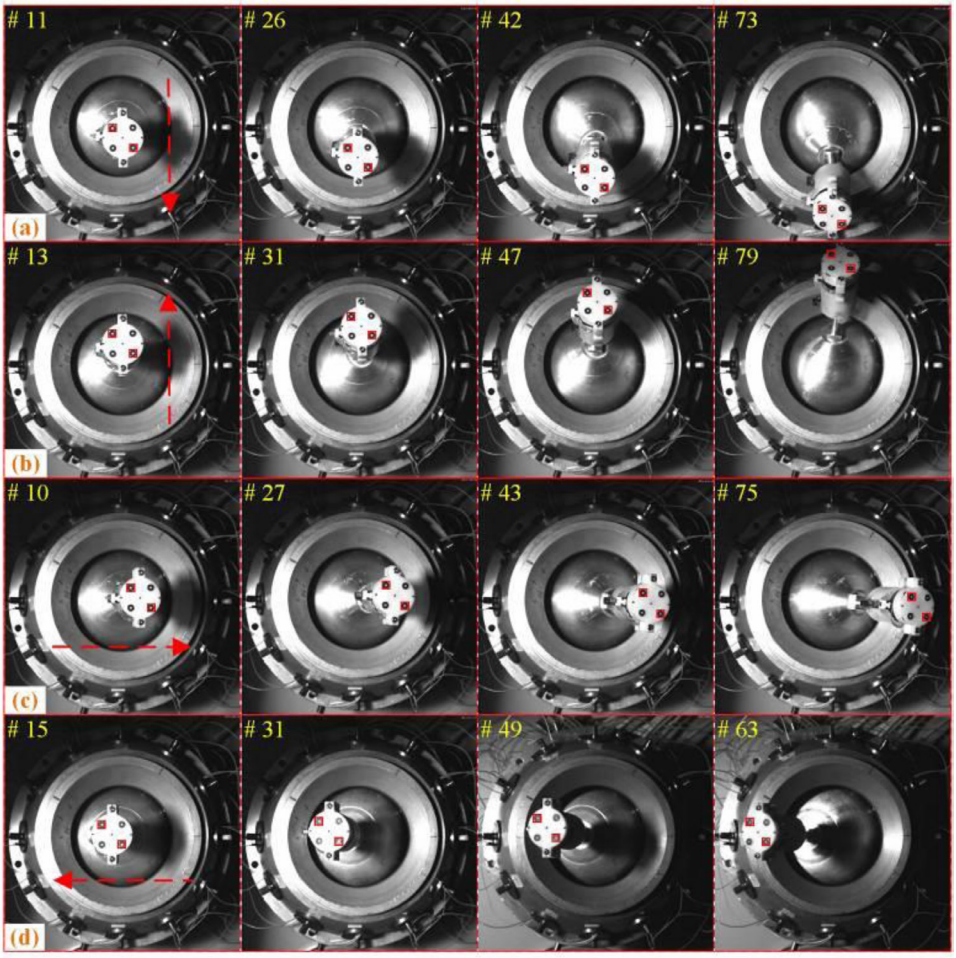

Figure 13. Some images from the video sequences of tilt motions: (a) $X+$, (b) $X-$, (c) $Y+$, (d) $Y-$.

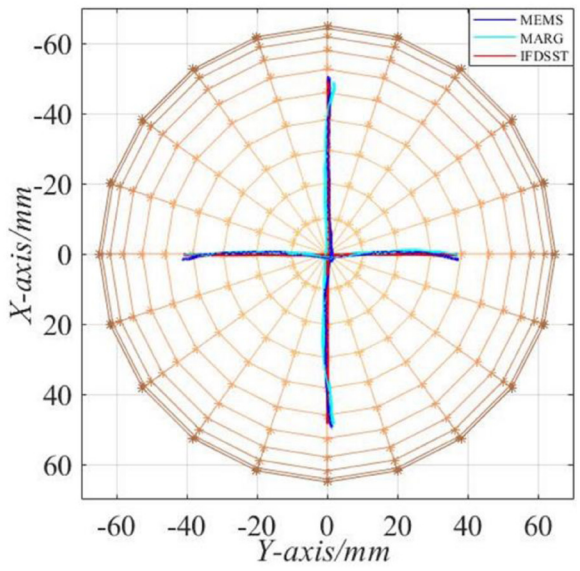

Figure 14. Trajectories from the MEMS sensor, FCF and the proposed IFDSST method in the tilt motion experiments (top view).

In all experiments, the average frame rate of the proposed algorithm can reach up to 92 frames per second, meeting the basic real-time requirements of tracking. The errors are analyzed mainly from two aspects: (1) the errors in the experiments are compared with the MEMS sensor and FCF estimation methods, and the installation error caused by the MEMS sensor device used on the output shaft is unavoidable. The estimated attitude in the three methods may be located at a different point on the end face of the output shaft; (2) The region where the target is detected is obtained using the proposed algorithm, and the center of the detected rectangular area is considered the target position. From the area to the point, an error may exist.

5.5. Discussions

To make the paper more explicit and flexible in practical applications, the factors that affect the performances of the proposed method are discussed as shown below:

5.5.1. Uncertainties of the vision capture system and feature extraction. The following factors from the vision capture system and the feature extraction may affect the accuracy of attitude estimation for PMSM: some parameters of the experimental platform, illumination variation and target deformation. For example, the distance from the lens to the rotor h_c is measured by artificial selection, which would affect the accuracy of attitude estimation. It is judged by the human eyes whether the center of the lens and the center of the output shaft

Table 5. The RMSEs of the trajectory positions for tilt motion from the MEMS sensor, FCF and the proposed IFDSST method.

Direction of tilt motion	MEMS (mm)	FCF (mm)	IFDSST (mm)
$X+$	0.963	1.224	0.183
$X-$	1.052	1.135	0.270
$Y+$	1.128	1.562	0.208
$Y-$	1.309	0.447	0.256
Average RMSE	1.113	1.092	0.229

are aligned along a straight line, which will lead to the inconsistency between the original center of the stator coordinate system and the center of the image. This will further affect the value of m and n and the calculation of the attitude angle. In practice, the illumination variation from the vision capture system is uneven. However, the proposed IFDSST used in this paper is to extract HOG features for the target, which is related to the change of pixel to grayscale. The light transformation will affect the extraction of HOG features and the accuracy of rotor attitude estimation. In addition, if the rotor moves too fast, the shape of the target may change, which will affect the feature extraction, feature matching, and ultimately the target detection and tracking. Therefore, the robustness of the algorithm against deformation and illumination should be further studied in the future.

5.5.2. Using Kalman filter to improve the tracking accuracy. The Kalman filter has the advantages of estimating and correcting the object motion state [37]. As an effective estimation algorithm, the Kalman filter is widely used in engineering applications such as radar and computer vision [38]. Hence, the covariance formula of the rotor motion state can be deduced and the Kalman filter can be integrated into the algorithm to improve the estimation accuracy in future work.

So far, the PMSM is in the open loop running state. However, the next step of motor research is to realize closed-loop control by combining the rotor's attitude estimation algorithm, and to study the motor's operation performance with load. When the load is columnar or the volume is small, such as the robot arm, the proposed IFDSST is available. In future research, the proposed attitude estimation algorithm can be integrated into the motor's control algorithm to realize closed-loop control and on-load operation.

6. Conclusion

In this study, a detection method based on the target tracking algorithm is proposed to estimate the attitude of a spherical motor rotor. The proposed method is based on the FDSST algorithm, which can realize motion tracking by extracting the HOG feature of the target in the video sequence. The method is made feasible for engineering applications of the motor by transforming the single-target tracking algorithm into a multi-target one under the premise of ensuring accuracy and robustness. The actual attitude of the motor's output shaft is calculated by tracking the markers and estimating the positions of the markers in the image. Based on the existing PMSM platform, we complete three experiments: yaw, spin, and tilt motion. In the experiments, we select the MEMS sensor and FCF for comparison to verify the feasibility of our algorithm. In the yaw motion, the average relative angle error of the proposed IFDSST algorithm is 1.0%, which is less than those of the MEMS and FCF methods (both around 1.5%). In the spin motion, the relative trajectory errors of the MEMS and FCF method are between 0.6% and 0.7%, while the error of the proposed IFDSST algorithm is 0.3%. In the tilt motion, the trajectory RMSEs of the MEMS and FCF methods are both over 1.0 mm, while the RMSE of the proposed IFDSST algorithm is about 0.2 mm. Experimental results show that the rotor attitude of the motor can be estimated effectively and accurately using the proposed algorithm.

Acknowledgments

This work was supported in part by the National Natural Science Foundation of China under Grant Nos. 51637001 and 51605002. The authors would like to thank the anonymous reviewers for their valuable comments and suggestions.

ORCID iDs

Qunjing Wang https://orcid.org/0000-0002-1916-8116
Siliang Lu https://orcid.org/0000-0002-7101-7948

References

[1] Cho S, Lim J S, Oh Y J, Jeong G, Kang D W and Lee J 2018 A study on output characteristics of the spherical multi-DOF motor according to the number of phases and pole pitch angles *IEEE Trans. Magn.* **54** 8205005
[2] Nakajima S, Kajiwara H, Aoyagi M, Tamura H and Takano T 2016 Study on spherical stator for multidegree-of-freedom ultrasonic motor *Japan. J. Appl. Phys.* **55** 07KE18
[3] Lu B, Aoyagi M, Takano T and Tamura H 2010 Examination of sandwich-type multidegree-of-freedom spherical ultrasonic motor *Japan. J. Appl. Phys.* **49** 07HE24
[4] Bai K, Xu R, Lee K-M, Dai W and Huang Y 2018 Design and development of a spherical motor for conformal printing of curved electronics *IEEE Trans. Ind. Electron.* **65** 9190–200
[5] Guo X, Li S, Wang Q, Wen Y and Gong N 2019 Dynamic analysis and current calculation of a permanent magnet spherical motor for point-to-point motion *IET Electric Power Appl.* **13** 426–34
[6] Yuan Q, Qian J, Wu H, Yin W and Jiang Q 2019 Stator current harmonic elimination control for the high-power synchronous motors with online implementation *IET Power Electron.* **12** 801–9
[7] Li H and Shen Y 2015 Thermal analysis of the permanent-magnet spherical motor *IEEE Trans. Energy Convers.* **30** 991–8
[8] Dias C G and Pereira F H 2018 Broken rotor bars detection in induction motors running at very low slip using a hall effect sensor *IEEE Sens. J.* **18** 4602–13
[9] Yang Y L, Wei Y D, Lou J Q, Fu L and Fang S 2017 Design and control of a multi-DOF micromanipulator dedicated

to multiscale micromanipulation *Smart Mater. Struct.* **26** 115016
[10] Fernandes J F P and Branco P J C 2016 The shell-like spherical induction motor for low-speed traction: electromagnetic design, analysis, and experimental tests *IEEE Trans. Ind. Electron.* **63** 4325–35
[11] Kasashima N, Ashida K, Yano T, Gofuku A and Shibata M 2016 Torque control method of an electromagnetic spherical motor using torque map *IEEE/ASME Trans. Mechatronics* **21** 2050–60
[12] Li B, Yu R, Li H and Li G 2014 Design considerations of a permanent magnetic spherical motor using spherical harmonics *IEEE Trans. Magn.* **50** 1–9
[13] Rong Y P, Wang Q J, Lu S L, Li G L, Lu Y and Xu J Z 2019 Improving attitude detection performance for spherical motors using a MEMS inertial measurement sensor *IET Electric Power Appl.* **13** 198–205
[14] Lu Y, Hu C G, Wang Q J, Hong Y, Shen W X and Zhou C Q 2018 A new rotor position measurement method for permanent magnet spherical motors *Appl. Sci.-Basel* **8** 2415
[15] Herman J and Bojkovski J 2018 Evaluation and uncertainties of an electric direct-drive motor test system with a mathematical model confirmation *Meas. Sci. Technol.* **29** 105904
[16] Du S, Hu J, Zhu Y and Zhang M 2018 A Hall sensor-based position measurement with on-line model parameters computation for permanent magnet synchronous linear motor *IEEE Sens. J.* **18** 5245–55
[17] Liu G, Chen B and Song X 2019 High-precision speed and position estimation based on hall vector frequency tracking for PMSM with bipolar Hall-effect sensors *IEEE Sens. J.* **19** 2347–55
[18] Rabani A and Challis R 2013 A low-cost viscometer based on a permanent magnet dc motor *Meas. Sci. Technol.* **24** 035304
[19] Liu X, Liu C and Pong P W T 2018 Velocity measurement technique for permanent magnet synchronous motors through external stray magnetic field sensing *IEEE Sens. J.* **18** 4013–21
[20] Nishijima T, Yamamoto A, Yasui H and Higuchi T 2006 A built-in displacement sensor for an electrostatic film motor *Meas. Sci. Technol.* **17** 2676–82
[21] Nakhaeinejad M and Bryant M D 2011 Observability analysis for model-based fault detection and sensor selection in induction motors *Meas. Sci. Technol.* **22** 075202
[22] Garner H, Klement M and Lee K-M 2001 Design and analysis of an absolute non-contact orientation sensor for wrist motion control *Proc. 2001 IEEE/ASME Int. Conf. on Advanced Intelligent Mechatronics.* vol 1 pp 69–74
[23] Qian Z, Wang Q J, Guo X W, Li G L and Ma S 2014 Research of orientation detection method for spherical motor and effect on pd control system based on machine vision *2014 17th Int. Conf. on Electrical Machines and Systems* pp 2186–91
[24] Cichon D, Psiuk R, Brauer H and Topfer H 2019 A Hall-sensor-based localization method with six degrees of freedom using unscented kalman filter *IEEE Sens. J.* **19** 2509–16
[25] Chirikjian G S and Stein D 1999 Kinematic design and commutation of a spherical stepper motor *IEEE/ASME Trans. Mechatronics* **4** 342–53
[26] Lee D V and Velinsky S A 2007 Analysis and experimental verification of a three-dimensional noncontacting angular motion sensor *IEEE/ASME Trans. Mechatronics* **12** 612–22
[27] Lee K M and Zhou D 2004 A real-time optical sensor for simultaneous measurement of three-DOF motions *IEEE/ASME Trans. Mechatronics* **9** 499–507
[28] Wang W, Wang J, Jewell G W and Howe D 2003 Design and control of a novel spherical permanent magnet actuator with three degrees of freedom *IEEE/ASME Trans. Mechatronics* **8** 457–68
[29] Wu J, Zhou Z B, Chen J J, Fourati H and Li R 2016 Fast complementary filter for attitude estimation using low-cost MARG sensors *IEEE Sens. J.* **16** 6997–7007
[30] Wu Y W, Sui Y and Wang G H 2017 Vision-based real-time aerial object localization and tracking for UAV sensing system *IEEE Access* **5** 23969–78
[31] Tian Y L, Feris R S, Liu H W, Hampapur A and Sun M T 2011 Robust detection of abandoned and removed objects in complex surveillance videos *IEEE Trans. Syst. Man Cybern.* C **41** 565–76
[32] Zhang S, Wang C, Chan S-C, Wei X and Ho C-H 2015 New object detection, tracking, and recognition approaches for video surveillance over camera network *IEEE Sens. J.* **15** 2679–91
[33] Zhang T, Xu C and Yang M H 2019 Learning multi-task correlation particle filters for visual tracking, *IEEE Trans. Pattern Anal. Mach. Intell.* **41** 365–78
[34] Sidike P, Asari V K and Alam M S 2016 Multiclass object detection with single query in hyperspectral imagery using class-associative spectral fringe-adjusted joint transform correlation *IEEE Trans. Geosci. Remote Sens.* **54** 1196–208
[35] Ruan W *et al* 2019 Multi-correlation filters with triangle-structure constraints for object tracking *IEEE Trans. Multimedia* **21** 1122–34
[36] Danelljan M, Hager G, Khan F S and Felsberg M 2017 Discriminative scale space tracking *IEEE Trans. Pattern Anal. Mach. Intell.* **39** 1561–75
[37] Zhou Z B, Li Y, Liu J N and Li G 2013 Equality constrained robust measurement fusion for adaptive kalman-filter-based heterogeneous multi-sensor navigation *IEEE Trans. Aerosp. Electron. Syst.* **49** 2146–57
[38] Zhou Z B, Li Y, Rizos C and Shen Y Z 2009 A robust integration of GPS and MEMS-INS through trajectory-constrained adaptive kalman filtering *Proc. 22nd Int. Technical Meeting of the Satellite Division of the Institute of Navigation* pp 995–1003